Chemical Science

ROYAL SOCIETY OF CHEMISTRY

EDGE ARTICLE

View Article Online
View Journal | View Issue

Cite this: *Chem. Sci.*, 2026, **17**, 7590

All publication charges for this article have been paid for by the Royal Society of Chemistry

Breaking the scaling relationship for oxygen reduction *via* amino-molecule-interface-mediated metallene electrocatalysts

Shuya Xu,[a] Yunyi Zhang,[a] Yukun Peng,[a] Jiawei Ke,[a] Xueheng Liu,[a] Chenglin Yan,[bc] Lifang Zhang,*[a] Tongfei Li *[a] and Tao Qian [a]

Received 10th October 2025
Accepted 10th February 2026

DOI: 10.1039/d5sc07852k

rsc.li/chemical-science

Developing highly stable and active Pd-based catalysts for the oxygen reduction reaction (ORR) is crucial for enabling the large-scale application of anion exchange membrane fuel cells (AEMFCs) in hydrogen utilization. However, the conventional oxygen associative pathway limits ORR efficiency due to the persistent scaling relationship. Unlike commonly reported alloying strategies, here we report a polyethyleneimine (PEI)-mediated interface engineering strategy to modify the PdRh metallene (PdRh@PEI) for efficient ORR catalysis and fuel cells. The PdRh@PEI catalyst exhibits a high half-wave potential ($E_{1/2}$) of 0.96 V (*vs.* RHE) and mass activity of 1.23 A mg_{Pd}^{-1} at 0.9 V, which is higher than that of the benchmark Pt/C and most reported Pd-based catalysts, certifying its top-level performance. *In situ* vibrational spectroscopy and computational investigations unveiled that the PEI modification donates electron density from PEI to the PdRh atoms, resulting in a pronounced downshift of the d-band center, a reduced activation barrier in the rate-limiting step, and enhanced oxygen dissociation from *OOH to *O *via* a dissociative mechanism. When utilized as a cathode in AEMFCs, PdRh@PEI demonstrates a high power density (164.3 mW cm^{-2}) and outstanding operational durability (over 24 h without voltage decay), highlighting the effectiveness of molecular interface modification in the design of efficient Pd-based metallenes for energy conversion applications.

Introduction

The escalating severity of the energy crisis and environmental pollution, driven by the extensive use of fossil fuels, has significantly heightened the demand for clean and efficient energy conversion and storage technologies.[1–4] Rechargeable battery systems, such as anion exchange membrane fuel cells (AEMFCs), have garnered considerable attention as viable alternatives because of their environmental friendliness, mature infrastructure and industry for H_2 utilization, reduced operating temperatures, and high energy density.[5–8] However, their performance is substantially limited by the slow kinetics of the cathodic oxygen reduction reaction (ORR) at the cathode, which involves multiple electron transfer processes such as O_2 activation, hydrogen adsorption, O–O bond cleavage, and hydroxyl group desorption.[9–12] These intermediates follow the scaling relationships $\Delta G_{*OOH} \approx \Delta G_{*OH} + 3.2$ eV and $\Delta G_{*O} \approx 2\Delta G_{*OH}$. Consequently, independent optimization of the binding energy for each intermediate presents a significant challenge, leading to a high theoretical overpotential required to drive the ORR and consequently impairing ORR activity.[13–15] According to the established free energy diagram of the ORR, the potential-determining step (PDS) is either the $O_2 \rightarrow$ *OOH transformation or the *OH $\rightarrow H_2O$ step. Given that the *OH $\rightarrow H_2O$ step is inevitable during the ORR, there is a critical need for practical strategies that circumvent *OOH formation and facilitate direct dissociation of adsorbed oxygen molecules ($*O_2$) into two *O species, thereby enhancing ORR performance.[16–18] However, achieving this goal requires the development of efficient electrocatalysts with strong O_2 adsorption capability—a longstanding challenge in the field.

Although Pt-based catalysts currently demonstrate superior ORR activity and favorable reaction kinetics, their large-scale commercial application suffers heavily from high costs, limited availability of Pt resources, and poisoning issues.[19,20] Palladium (Pd)-based metallenes, as an emerging class of two-dimensional materials, have shown great promise in ORR catalysis due to their unique physicochemical properties, featuring a high specific surface area, abundant surface unsaturated atoms, and tunable electronic structures. Pd and Pt belong to the same platinum group elements and share similar lattice parameters and electronic configurations; the advantage is that Pd is more

[a]*School of Chemistry and Chemical Engineering, Nantong University, Nantong 226019, China. E-mail: lfzhang@ntu.edu.cn; litongfei@ntu.edu.cn*

[b]*School of Petrochemical Engineering, Changzhou University, Changzhou 213164, China*

[c]*College of Energy, Key Laboratory of Core Technology of High Specific Energy Battery and Key Materials for Petroleum and Chemical Industry, Soochow University, Suzhou 215006, China*

abundant and less expensive than Pt.[21–25] More importantly, the catalytic performance of Pd-based metallenes can be further enhanced through strategies such as strain engineering, alloying, and interface modulation. Research advances have demonstrated that alloying Pd with a second metal (*e.g.*, Rh, Cu, Au, or Hf) effectively tunes the d-band center of Pd, optimizes the adsorption strength of oxygen-containing intermediates on the catalyst surface, and thereby significantly improves intrinsic ORR activity.[26–30] For instance, in our previous work, we synthesized a PdRhCu metallene that exhibited outstanding performance in acidic ORR, achieving an $E_{1/2}$ of up to 0.93 V.[31] Despite the remarkable promise of Pd-based metallene materials, their practical deployment continues to confront two pivotal challenges: the delicate trade-off between catalytic activity and long-term stability, and inadequate tolerance toward methanol crossover. In alkaline environments, conventional Pd-based catalysts demonstrate moderate ORR activity, yet they frequently fall short in harmonizing high performance with enduring durability.[32–36] On the other hand, it is important to recognize that the strong attractive forces among surface atoms in metallenes naturally lead to compressive strain, resulting in relatively weak binding affinity for $*O_2$. This poses a considerable obstacle for initiating the oxygen dissociation process in metallenes, as doing so involves surmounting a moderate activation energy barrier.[37–39] Unlike the commonly reported atomic-level design, constructing polymer molecular-level modifications near the catalyst surface can not only regulate the electronic structure and surface adsorption behavior but also modulate the interfacial microenvironment between the electrode and electrolyte, thereby enhancing mass transfer efficiency.[40–44] Nevertheless, a fundamental understanding of how the polymer influences catalyst properties and the reaction mechanism remains essential and requires further investigation.

Based on these considerations, we herein present a novel PdRh@PEI metallene designed to significantly enhance the ORR in alkaline media by breaking the scaling relationship in the traditional oxygen associated mechanism through the amine functionality of PEI molecules. PEI was selected due to its characteristics as an amino-rich polymer modifier, which endows it with strong electron-donating capacity and effective metal-coordinating ability during the fabrication process. The as-developed PdRh@PEI metallene exhibits exceptional electrocatalytic activity and durability, outperforming both its binary metallene counterparts and commercial Pt/C. It demonstrates a high half-wave potential ($E_{1/2} = 0.96$ V *vs.* RHE), negligible activity loss after 10 000 cycles, and strong resistance to CO poisoning, positioning it among the top-tier materials compared to previously reported Pd-based catalysts. Sophisticated theoretical simulations reveal that interface engineering mediated by PEI induces a profound redistribution of electronic charge from PEI to the PdRh metallene, culminating in pronounced electron enrichment at Pd active sites and a distinct downshift of the d-band center. This electronic modulation effectively weakens the adsorption of oxygen-containing intermediates, confers exceptional CO tolerance, and thereby optimally tunes the reaction energetics and promotes the direct dissociation of O_2, facilitating a more favorable pathway for the ORR. *In situ* Fourier transform infrared (FTIR) spectroscopy demonstrates that the PEI molecule shifts the reaction pathway from "associative" to "dissociative" and facilitates the dissociative pathway of oxygen from *OOH to *O. Beyond that, the catalyst exhibits an exceptional power density of 164.3 mW cm^{-2} at a current density of 365 mA cm^{-2}, significantly outperforming the Pt/C-based control device, which achieves only 94.8 mW cm^{-2} at 300 mA cm^{-2} when equipped into a membrane electrode assembly in an AEMFC. To the best of our knowledge, this represents the first documented utilization of molecular-level modification on Pd-based metallenes as a cathode material in AEMFCs, marking a pioneering advancement in the field.

Results and discussion

Initially, we utilized theoretical computations to forecast the potential positive influences of the PEI molecule on the PdRh alloy structure. To decipher the atomic-level origin of the enhanced ORR activity in the PdRh@PEI metallene when compared with unadorned PdRh sites, the first-principles density functional theory (DFT) simulations were systematically implemented across three critical dimensions: electronic structure evolution, thermodynamic pathway analysis, and adsorption descriptor correlations. Based on the atomic arrangement information, the theoretical configurations of PdRh@PEI and PdRh have been meticulously proposed (Fig. S1). The initial charge density difference mapping (Fig. 1a) result reveals interfacial charge redistribution characteristics, with pronounced electron accumulation (yellow isosurfaces) over the PdRh metallene and depletion regions (green isosurfaces) near PEI moieties. This directional electron transfer, quantified at 0.32 e^- $Å^{-2}$ through Bader analysis, arises from the synergistic interplay between the metal's work function ($\Phi_{PdRh} = 4.85$ eV) and PEI's electron-donating amine groups ($\Delta\Phi = 0.41$ eV). This outcome makes the PdRh atoms adopt an electron-rich configuration. Such a redistribution of charge modifies the bonding behavior of the PdRh catalyst. The

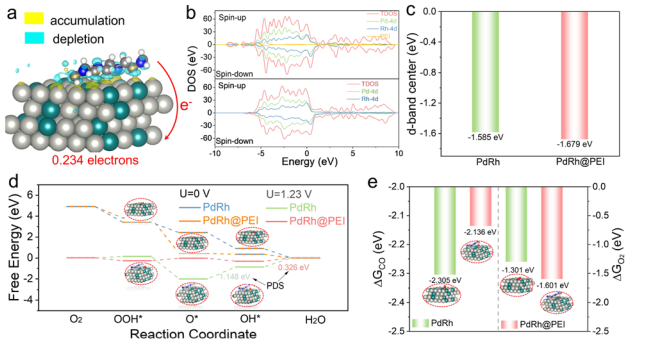

Fig. 1 Mechanism study by DFT calculations. (a) Differential charge density profile for PdRh@PEI. (b) PDOS of PdRh@PEI and PdRh. (c) Projected d-band center. (d) Free energy profiles of key intermediates for PdRh@PEI and PdRh at an overpotential of $U = 0$ V and 1.23 V. (e) CO and O_2 adsorption energies on different catalytic sites.

interaction between the catalyst's surface atoms and the adsorbates causes the formation of bonding orbitals at lower energy levels and antibonding orbitals at elevated energy levels. Comprehensive projected density of states (PDOS) analysis (Fig. 1b) demonstrates that PEI coordination induces (i) a 134 meV negative shift in Pd-4d orbitals *via* ligand-to-metal charge transfer, and (ii) d-band broadening (FWHM increases from 3.28 eV to 3.51 eV) through enhanced Pd–Rh orbital hybridization. Meanwhile, the metallic nature of the PdRh@PEI conductor was evidenced by the dominance of Pd 4d and Rh 4d electronic states at the Fermi level (E_F), which is consistent with previously reported results.[45] The pronounced downshift in the d-band center ($\Delta\varepsilon_d = -94$ meV, as illustrated in Fig. 1c) exerts a profound modulation on the occupancy of antibonding states. This phenomenon, which may be attributed to the lone pair electrons of the $-NH_2$ group effectively donating electron density to the PdRh atoms, significantly reduces the binding affinity of $*O_2$ compared to that of pristine PdRh.[46] In the PdRh-based system, at a potential of 0 V *versus* RHE, all stages of the reaction unfold in an exergonic manner on both catalytic surfaces, revealing a thermodynamically favorable progression throughout. The potential-dependent Gibbs free energy landscapes (Fig. 1d) identify the O* → OH* transition as the potential-determining step (PDS) for PdRh, whereas PdRh@PEI exhibits a substantially reduced activation barrier ($\Delta G = 0.326$ eV *vs.* 1.148 eV) and features the OH* → H_2O transition as its PDS. This reduction stems from the optimized *O adsorption configuration enabled by PEI-mediated surface polarization. To validate the potential dissociation mechanism, we have augmented our analysis with a comprehensive calculation of the full $4e^-$ reduction pathway ($O_2 \rightarrow 2O \rightarrow 2OH \rightarrow 2H_2O$). The results reveal two pivotal insights: (1) the cleavage of the O–O bond emerges as a thermodynamically and kinetically favored process on the PdRh@PEI surface, offering robust theoretical support to the *in situ* spectroscopic evidence (the following section will discuss this); (2) nevertheless, the hydrogenation step—specifically O to OH (or OH to H_2O)—remains the potential determining bottleneck of the entire pathway. This indicates that while the initial O_2 activation undergoes a mechanistic transition from an associative to a dissociative route, the overall reaction kinetics are still governed by the same limiting barrier as before. Crucially, the energy landscape remains consistent with prior conclusions, affirming the reliability and coherence of our mechanistic framework (Fig. S2). Adsorption descriptor analysis (Fig. 1e) further establishes that dual functionality (1) weakened CO* binding ($\Delta E_{ads} = -2.136$ eV for PdRh@PEI *vs.* −2.305 eV for PdRh) through Pauli repulsion enhancement (charge depletion at the CO σ-orbital), indicating a significant reduction in the level of CO poisoning and (2) enhanced O_2* dissociation ($E_{ads} = -1.601$ eV) *via* strengthened π-backdonation (metal → O_2 π* orbital occupancy). Remarkably, upon PEI functionalization, the average d-band center of these active centers ascended from −1.475 eV to −1.429 eV-drawing nearer to the Fermi level. This subtle yet significant modulation of the local electronic structure aligns seamlessly with the experimentally observed enhancement in $*O_2$/*OOH adsorption affinity, fully corroborating the predictions of d-band center theory (Fig. S3). Moreover, it reveals that the overall downward shift and the localized upward shift pertain to distinct hierarchical levels of electronic response, coexisting harmoniously without contradiction. The synergy between electronic structure modulation and adsorption site engineering creates an optimal Sabatier volcano position, rationalizing the specific activity enhancement. These findings establish PEI as a multifunctional co-catalyst that simultaneously tailors the electronic structure, stabilizes reaction intermediates, and prevents catalyst poisoning.

Guided by the aforementioned theoretical predictions, we achieved the successful synthesis of the PdRh@PEI sample, with the detailed experimental procedure meticulously outlined in the Experimental section. The overall morphology of the PdRh@PEI metallene was meticulously characterized by scanning electron microscopy (SEM), transmission electron microscopy (TEM), and high-angle annular dark-field scanning transmission electron microscopy (HAADF-STEM). As shown in Fig. 2a, b and S4, the PdRh@PEI metallene displayed an exceptionally delicate, ultra-thin, and intricately crumpled two-dimensional graphene-like nanosheet structure, characterized by irregular morphologies and gently curled edges, with an average lateral dimension extending to several hundred nanometers. Observing the folded edge of the PdRh@PEI metallene, one can discern a thickness of approximately 1.93 nm, a compelling testament to the successful fabrication of a multilayer, metal-stacked metallene architecture (Fig. S5). The high-magnification TEM image further reveals the presence of a delicate, ultra-thin PEI layer, measuring ~1.4 nm in thickness,

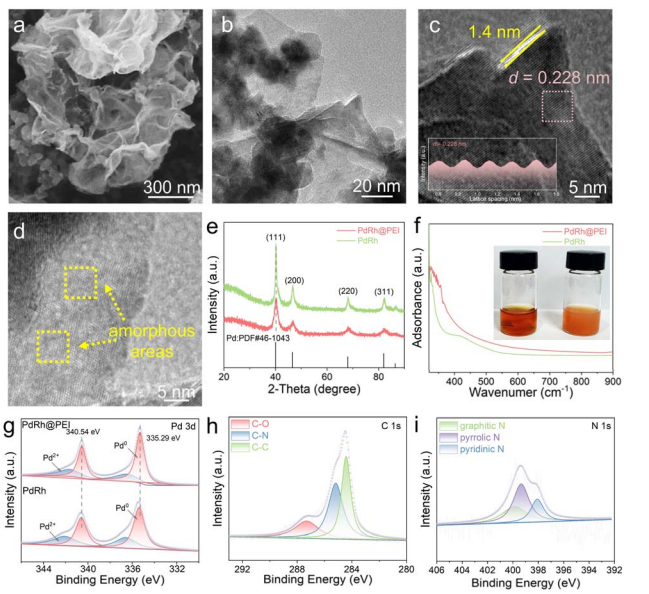

Fig. 2 Morphology and phase characterization of PdRh@PEI: (a) SEM image. (b) TEM image. (c) HRTEM image with an inset showing lattice spacing. (d) Additional HRTEM image. (e) XRD patterns. (f) UV-vis absorption spectra of PdRh@PEI and PdRh solution (photograph showing PdRh solution (left) and PdRh@PEI solution (right)). (g) XPS spectra of the Pd 3d region. (h) XPS spectra of the C 1s region. (i) XPS spectra of the N 1s region.

gracefully enveloping the edges of the PdRh metallene structure. The high-resolution transmission electron microscopy (HRTEM) image of the PdRh@PEI metallene presents a distinct lattice fringe with an interplanar spacing of 0.228 nm (Fig. 2c), notably exceeding the standard *d*-spacing of the Pd (111) plane at 0.224 nm. This deviation may be attributed to the electronic modulation induced by the alloying effect. High-resolution transmission electron microscopy (HRTEM) reveals the presence of localized amorphous regions on the surface of PdRh alloys, potentially indicative of PEI molecular adsorption (Fig. 2d). As evident from the HAADF-STEM and elemental mapping images (Fig. S6), the Pd, Rh, C, and N elements are exquisitely and uniformly dispersed across the entire PdRh@PEI metallo-molecular framework, offering compelling evidence that the PEI molecules have been effectively grafted onto the metallene surface. In addition, the weight ratio of Pd to Rh in the PdRh@PEI metallene was precisely determined to be 67.53–17.58 through inductively coupled plasma optical emission spectrometry (ICP-OES), as summarized in Table S1. Moreover, the highly hydrophilic PdRh@PEI metallene surface demonstrated rapid water droplet absorption, as shown by contact angle measurements taken before and 1 s after water exposure (Fig. S7), clearly reflecting the catalyst's strong affinity for water and excellent wetting properties. In contrast, the PdRh surface exhibited a contact angle of 16.257° (Fig. S8), indicating markedly reduced hydrophilicity in the absence of PEI surface modification.

The crystal structure of the PdRh@PEI metallene was analyzed using powder X-ray diffraction (XRD). The XRD pattern of the PdRh metallene exhibited four distinct diffraction peaks at 40.3°, 46.7°, 68.2° and 82.5°, which correspond to the (111), (200), (220) and (311) crystallographic planes of Pd (JCPDS-46-1043), respectively (Fig. 2e). After the deposition of the PEI layer, the XRD pattern of the PdRh@PEI metallene showed no significant shift in peak positions, indicating the formation of a thin amorphous PEI layer on the surface of the the PdRh metallene. To further investigate the interaction of PEI within the PdRh@PEI system, a comprehensive set of control experiments was conducted. Upon the addition of PEI to solutions of K_2PdCl_4 and $RhCl_3$, an immediate formation of a turbid orange-colored solution was observed. This phenomenon suggests that the amine ($-NH_2$) groups present in PEI may engage in coordination with the metal ions in K_2PdCl_4 and $RhCl_3$, leading to the formation of a PEI-Pd^{2+}–Rh^{3+} complex (Fig. 2f). This hypothesis was further substantiated through UV-vis spectroscopy and linear sweep voltammetry (LSV) analyses (Fig. S9). Following the introduction of PEI, a distinct blue shift was observed in the UV-vis absorption spectrum, providing strong evidence for the formation of the aforementioned complex. Moreover, in comparison to the K_2PdCl_4 + $RhCl_3$ solution, the reduction peak potential of the PEI + K_2PdCl_4 + $RhCl_3$ mixture exhibited a noticeable negative shift, further supporting the coordination interaction. The molecular architecture of PEI was elucidated *via* Fourier-transform infrared (FT-IR) spectroscopy (Fig. S10), revealing the characteristic features of branched PEI (molecular weight: 1200). That is, the spectrum displayed a broad N–H stretching vibration at 3282 cm^{-1}, prominent and sharp C–H stretching double peaks at 2860 and 2920 cm^{-1}, a distinct primary amine bending vibration peak at 1600 cm^{-1}, a strong in-plane bending vibration peak attributed to C–H at 1460 cm^{-1}, and a C–N stretching vibration peak within the range of 1100–1300 cm^{-1}. The elemental composition and surface valence states of PdRh@PEI were thoroughly examined using X-ray photoelectron spectroscopy (XPS). The XPS survey spectrum of PdRh@PEI (Fig. S11) distinctly reveals the presence of C, N, Rh, and Pd, underscoring the successful integration of these elements within the material's architecture. In the XPS Pd 3d spectrum of the PdRh metallene, two prominent peaks at 335.38 and 340.60 eV are assigned to the Pd^0 $3d_{5/2}$ and Pd^0 $3d_{3/2}$ orbitals, respectively. Additionally, two other peaks at 336.62 and 342.16 eV indicate the presence of Pd^{2+} species, which may result from partial oxidation of the catalyst upon exposure to air. Following PEI modification, the binding energy of the Pd^0 $3d_{5/2}$ peak (335.28 eV) for PdRh@PEI shows a negative shift of 0.1 eV compared to the unmodified PdRh metallene (Fig. 2g). In the Rh 3d profiles of the PdRh metallene, two prominent peaks at 305.91 and 311.14 eV are clearly assigned to the Rh^0 $3d_{5/2}$ and Rh^0 $3d_{3/2}$ orbitals, respectively. Upon modification with PEI, the Rh^0 $3d_{5/2}$ signal of PdRh@PEI exhibits a noticeable negative shift of 0.33 eV, decreasing from 305.91 eV in the pristine PdRh metallene to 305.58 eV (Fig. S12). This spectral shift can be attributed to the electron-donating effect of the lone pairs present in the amino groups of PEI molecules, which effectively transfer electrons to the PdRh metallene framework, thereby altering its electronic environment. In the C 1s XPS spectrum, three distinct peaks at 284.45, 285.19, and 287.33 eV are attributed to C–C, C–N, and C–O bonding configurations, respectively (Fig. 2h). With regard to the N 1s XPS spectrum, the binding energies observed at 399.90, 399.35 and 398.09 eV are correspondingly attributed to graphitic N, pyrrolic N and pyridinic N species, respectively (Fig. 2i). Based on the analysis of peak areas, it is evident that PdRh@PEI predominantly contains pyridinic nitrogen (46.6%) and pyrrolic nitrogen (22.6%), both of which are known to facilitate the catalytic ORR through an efficient four-electron transfer pathway. Collectively, these findings provide compelling evidence for the successful functionalization of PEI on the PdRh metallene surface, which is then anticipated to boost the electrochemical properties.

Owing to the remarkable coordinating ability of the –NH– and $-NH_2$ groups in PEI, a portion of PEI molecules becomes selectively adsorbed onto the surface of the synthesized noble metal nanocrystals, resulting in PEI-functionalized noble metal nanocrystals. This dual-functional architecture is expected to significantly enhance the ORR performance through synergistic effects of electronic modulation and surface functionalization. For comparative analysis, the PdRh metallene (Fig. S13) and commercially available Pt/C were subjected to identical measurement conditions to ensure a comprehensive evaluation. The electrocatalytic ORR activity was assessed using a rotating disk electrode (RDE). Prior to activity measurements, cyclic voltammetry (CV) was performed in N_2- and O_2-saturated 0.1 M KOH solutions at a scan rate of 50 mV s^{-1} (Fig. S14 and S15). All of these samples exhibited remarkable oxygen reduction capability, which were verified by comparing them against

a N_2-saturated environment used as a reference. By integrating the PdO reduction peak from the CV curves, the electrochemically active surface area (ECSA) of the Pd-based catalysts was calculated, as illustrated in Fig. S16. Remarkably, PdRh@PEI displayed the highest ECSA of 12.2 cm^2, significantly outperforming the PdRh metallene, which exhibited an ECSA of 8.16 cm^2. Linear sweep voltammetry (LSV) curves were subsequently obtained in O_2-saturated 0.1 M KOH at a scan rate of 10 mV s^{-1} to evaluate ORR performance. As depicted in Fig. 3a and b, PdRh@PEI demonstrated a half-wave potential ($E_{1/2}$) of 0.96 V *vs.* RHE, outperforming PdRh@PEI-600 (0.85 V), PdRh@PEI-1800 (0.83 V), PdRh metallene (0.77 V), and commercial Pt/C (0.85 V), indicating superior ORR activity among all samples. It can be observed that the enhancement is specific to the PdRh@PEI sample (with mid-range molecular weight, *e.g.*, ~1200 in our case). We attribute this to an optimal interplay between PEI loading, the polymer chain conformation, and electronic metal–support interaction (EMSI). The PEI molecular weight directly governs its chain length and conformation on the catalyst surface. With the low M_w (*e.g.*, PdRh@PEI-600), shorter chains may form a sparse, incomplete layer. This provides an insufficient ligand-field effect to significantly modulate the electronic structure of the PdRh nanoparticles. With the optimal M_w (PdRh@PEI), the medium-length chains can form a dense, uniform, and positively charged monolayer. This optimal coverage achieves two key effects: (1) it creates a strong interfacial electronic interaction, effectively withdrawing electrons from the metal surface (as confirmed by our XPS analysis, which shows a positive shift in the Pd 3d binding energy), optimizing the binding energy of oxygen intermediates. (2) It forms a hydrophilic nano-environment that facilitates OH^- transfer, without physically blocking the access of small O_2 molecules to the active sites. When it comes to the high M_w (*e.g.*, PdRh@PEI-1800), the long, entangled polymer chains are more likely to form a thick, dense layer that can physically block the active sites, hindering mass transport of O_2 to the metal surface and thereby reducing the apparent activity. This "blocking effect" counteracts the beneficial electronic effect. Furthermore, PdRh@PEI exhibited the smallest Tafel slope of 83.13 mV dec^{-1}, compared to 95.54, 90.53, 100.82, and 88.01 mV dec^{-1} for PdRh@PEI-600, PdRh@PEI 1800, PdRh metallene, and Pt/C, respectively (Fig. 3c), suggesting accelerated ORR kinetics. The mass activity, normalized to both Pd mass and ECSA, was used to quantify the intrinsic ORR performance. At 0.9 V *vs.* RHE, PdRh@PEI delivered a mass activity of 1.23 A mg_{Pd}^{-1}, which is 24.6 times higher than that of the PdRh metallene (0.05 A mg_{Pd}^{-1}) (Fig. S16). To investigate the influence of amino group content and composition in amino-containing molecules on the PdRh alloy, XPS was employed. The N 1s spectra revealed that the contents of pyrrolic N in PdRh@PEI prepared with PEI of molecular weights of 600 and 1800 were 33.9% and 40.6%, respectively, while pyridinic N accounted for 23.7% and 37.6%, respectively (Fig. S17 and S18). Notably, PdRh@PEI possessed the highest concentrations of both pyrrolic and pyridinic N, consistent with its exceptional ORR performance. Additionally, CO stripping experiments were performed to evaluate tolerance to CO poisoning. The CO oxidation peaks for PdRh@PEI, PdRh metallene, and commercial Pt/C appeared at 0.664, 0.682, and 0.705 V, respectively, indicating enhanced CO oxidation capability on PdRh@PEI (Fig. 3d). Overall, PdRh@PEI demonstrates outstanding electrochemical performance, particularly in $E_{1/2}$ and mass activity, surpassing most reported Pt- and Pd-based electrocatalysts (Fig. 3f, and Table S2), thereby positioning it among the state-of-the-art ORR catalysts.

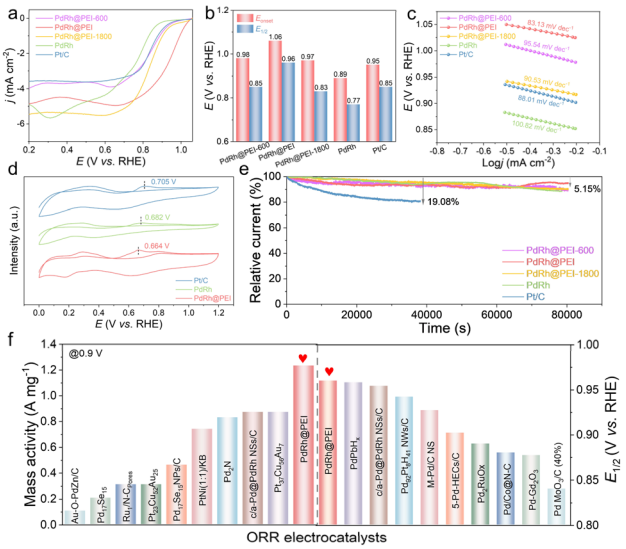

Fig. 3 Electrochemical evaluation of PdRh@PEI with different molecular weights, PdRh and commercial Pt/C under alkaline conditions (O_2-saturated 0.1 M KOH electrolyte). (a) LSV curves. (b) Statistics for E_0 and $E_{1/2}$. (c) Tafel plots. (d) CO stripping voltammograms. (e) Chronoamperometric curves. (f) Summary of the $E_{1/2}$ and MA values for PdRh@PEI and those of previously reported advanced Pt- and Pd-based ORR catalysts.

To elucidate the influence of PEI on the ORR performance of the PdRh metallene, systematic investigations were carried out by varying both the amount of PEI used during synthesis and the reaction time. First, the effect of PEI dosage was examined while maintaining a constant molecular weight. Compared to the previously optimized dosage of 8 mg, additional amounts of 4, 6, and 10 mg were evaluated. The $E_{1/2}$ values decreased in the order: 8 mg (0.96 V) > 10 mg (0.84 V) > 4 mg (0.82 V) > 6 mg (0.78 V). Consistent with earlier results, the catalyst prepared with 8 mg of PEI exhibited the most favorable performance, including a high onset potential (E_0) of 1.06 V and an $E_{1/2}$ of 0.96 V (Fig. S19–S21). Furthermore, a time-dependent study was conducted to assess the evolution of catalytic performance over synthesis durations ranging from 2 to 6 h. The results indicated that catalysts synthesized within 4 h achieved significantly superior E_0 and $E_{1/2}$ values compared to those obtained at 2 and 6 h (Fig. S22–S24), suggesting the existence of an optimal reaction window for achieving the optimal ORR activity.

In addition to activity, stability represents a critical metric for assessing the overall catalytic performance. Accelerated durability tests (ADTs) were therefore conducted by cycling the potential between 0.6 and 1.0 V *vs.* RHE at 200 mV s^{-1} in O_2-saturated 0.1 M KOH. LSV recorded before and after 10 000 cycles revealed a negligible shift in the $E_{1/2}$ for PdRh@PEI

(Fig. S25). In contrast, significant negative shifts were observed for PdRh@PEI-600 (19 mV), PdRh@PEI-1800 (10 mV), PdRh metallene (12 mV), and commercial Pt/C (10 mV) (Fig. S26–S28). Long-term stability was further evaluated *via* chronoamperometry at 0.4 V *vs.* RHE over 86 400 s. PdRh@PEI, along with PdRh@PEI-600, PdRh@PEI-1800, and the PdRh metallene, retained approximately 94.85% of their initial current density, indicating excellent operational stability. Under identical conditions, commercial Pt/C suffered a pronounced current loss of ~19.08%, underscoring the superior stability conferred by the PEI modification (Fig. 3e). XPS analysis was performed on the PdRh@PEI sample following rigorous long-term stability testing (Fig. S29). In comparison with the pristine catalyst, the core-level spectra of Pd 3d exhibited negligible shifts in both binding energy peak positions and spectral profiles, while the N 1s signal-characteristic of PEI-remained distinctly detectable. To investigate the potential dissolution of the Pd and Rh elements during the electrochemical reaction process, we performed ADT on both PdRh@PEI and pristine PdRh catalysts. Following 10 000 potential cycles, the electrolyte was analyzed *via* ICP-OES to detect any metal leaching. As illustrated in Fig. S30, the concentrations of Pd and Rh leached from the unmodified PdRh accounted for 2% and 1.9% of the initial alloy content, respectively. In stark contrast, the PdRh@PEI system exhibited significantly reduced leaching, with only 1.3% of Pd and a remarkably low 0.65% of Rh released into the solution. These findings strongly indicate that the PdRh@PEI architecture effectively suppresses metal dissolution during prolonged electrochemical operation, thereby preserving catalytic integrity and serving as a key factor underlying its superior stability and sustained activity. Moreover, methanol tolerance tests conducted in 0.1 M KOH with 3 M methanol demonstrated that PdRh@PEI retained nearly 100% of its current density, whereas commercial Pt/C and the PdRh metallene experienced almost complete current decay (Fig. S31). This exceptional methanol crossover resistance-coupled with high activity, durability, and structural stability-establishes PdRh@PEI as a promising electrocatalyst for advanced fuel cell applications.

To elucidate the origin of the high catalytic activity and underlying reaction mechanisms of the PdRh@PEI metallene, we conducted *in situ* attenuated total reflection Fourier transform infrared absorption spectroscopy (ATR-FTIR) to monitor changes in oxygen intermediate species and the chemical bonding between catalyst active sites and oxygen adsorbates under operating ORR conditions at various applied potentials. Measurements were performed using a custom-designed electrochemical cell. To ensure uniform catalyst distribution and sufficient IR penetration, a stainless-steel electrode pedestal with a diamond window was employed as the working electrode, with the catalyst loading optimized to 1.0 mg cm^{-2}. For the ORR process, spectra were collected from 1.0 to 0.4 V *vs.* RHE in 0.1 M KOH. The PdRh metallene displayed distinct absorption bands at 890 and 1053 cm^{-1}, assignable to *O and *OOH species, respectively (Fig. 4a). PdRh exhibits a significantly enhanced *OOH signal, indicating that the surface ORR primarily follows the associative pathway, while the detection of

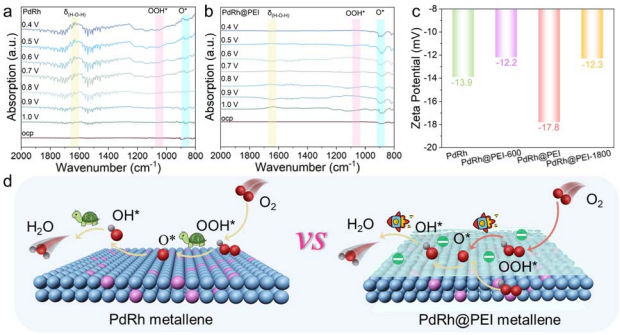

Fig. 4 (a) *In situ* ATR-FTIR spectra of PdRh and (b) PdRh@PEI recorded in an O_2-saturated 0.1 M KOH solution during the ORR process. (c) Zeta potential measurements. (d) Schematic illustration of the catalytic mechanism of PdRh@PEI compared to the conventional catalytic mechanism of PdRh for the ORR.

HOOH suggests that the dehydrogenation step of *OOH is inhibited, resulting in slower reaction kinetics and reduced catalyst stability. In contrast, no obvious *OOH signal was detected on PdRh@PEI, providing direct evidence that the reaction pathway shifted from "associative" to "dissociative". In addition, the characteristic peak between 1550 and 1650 cm^{-1} is attributed to the bending peak of water (δ_{H-O-H}). Compared with PdRh@PEI, PdRh exhibits a stronger water adsorption peak, indicating that PEI modulation significantly enhances interfacial water removal, thereby promoting the overall conversion process and increasing the reaction rate. In comparison, the PdRh@PEI metallene catalyst exhibited analogous vibrational features, yet with markedly enhanced peak intensities of *O (Fig. 4b), signifying accelerated reaction kinetics and improved catalytic activity relative to its pristine counterpart. Specifically, the intensity of the O–O stretching vibration peak of the *O species at 890 cm^{-1} gradually increases with the negative shift of the potential, which confirms that the PdRh alloy sites modified by the PEI molecule promote the rapid dissociation of *OOH to generate *O, a key intermediate in the four-electron pathway. Meanwhile, we have supplemented the ATR-FTIR data of samples prepared with a lower amount of PEI (4 mg and 6 mg, respectively), namely the PdRh@PEI metallene (4 mg) and PdRh@PEI metallene (6 mg). Compared with the PdRh and PdRh@PEI samples provided in the original text, the increase in PEI content does indeed accelerate the dissociation of *OOH to generate *O with the gradual enhancement of amino functionalization (Fig. S32). The site blocking effect becomes more obvious only when the addition amount of PEI exceeds 8 mg, rather than that in our standard samples. The zeta potential of PdRh@PEI (−17.8 mV) exhibits a significantly higher negative surface charge compared to PdRh (−13.9 mV), PdRh@PEI-600 (−12.2 mV), and PdRh@PEI-800 (−12.3 mV), as illustrated in Fig. 4c. The negative shift in zeta potential is a direct and inevitable consequence of amino functionalization, attributable to the amino group ($-NH_2$) acting as a Lewis base with strong electron-donating character and nucleophilicity. This electron donation modulates the electronic structure of the PdRh alloy and

systematically weakens the adsorption strength of key oxygen-containing intermediates (*OOH, *O, and *OH) at the active sites. Such attenuation optimally tunes the binding energy of the over-stabilized intermediates-particularly *OH, the precursor to OH^--toward a more favorable regime, thereby significantly lowering the desorption energy barrier and enhancing the overall ORR kinetics. These experimental findings are in excellent agreement with the reaction pathway deduced from DFT calculations, further corroborating the proposed mechanistic framework depicted in Fig. 4d.

In view of the excellent ORR performance and to rigorously evaluate the practical feasibility of the PdRh@PEI metallene within next-generation energy architectures, we meticulously engineered membrane electrode assemblies (MEAs) by integrating PdRh@PEI metallene-based cathodes with state-of-the-art Pt/C anodes, followed by a comprehensive assessment of alkaline fuel cell performance through polarization curve analysis and durability evaluation under realistic operational conditions. In the case of our custom-designed anion-exchange membrane fuel cell (AEMFC), the intricately refined assembly configuration is vividly illustrated in Fig. 5a, offering a lucid visualization of its architectural sophistication and functional precision. Notably, this dual-electrode system achieves an impressive open-circuit voltage of 1.03 V and delivers a peak power density of 164.3 mW cm^{-2} that markedly surpass those of commercial Pt/C and the PdRh metallene, which exhibit only 1.03 V and 94.8 mW cm^{-2}, 0.92 V and 66.5 mW cm^{-2}, respectively (Fig. 5b). The electrochemical impedance spectroscopy (EIS) profile, recorded at a current density of 250 mA cm^{-2} and depicted in Fig. 5c, reveals that the PdRh@PEI metallene-based MEA exhibits significantly reduced charge transfer resistance when compared to Pt/C and PdRh-containing MEAs. Furthermore, PdRh@PEI demonstrates an expanded electrochemically active surface area relative to the unmodified PdRh electrode, underscoring its enhanced catalytic accessibility. Cyclic voltammetry (CV) curves, presented in Fig. 5d, were employed to probe the oxygen reduction kinetics at both electrodes, further corroborating the superior interfacial reactivity of the PdRh@PEI metallene to that of PdRh and Pt/C. Collectively, these results unequivocally highlight the exceptional and distinctive cathodic activity of the PdRh@PEI metallene, positioning it as a highly promising candidate for advanced electrocatalytic systems. Remarkably, the AEMFC incorporating PdRh@PEI metallene exhibits outstanding operational stability, sustaining continuous and stable performance over 24 h at a current density of 250 mA cm^{-2} (Fig. 5e), demonstrating the promising practical application in AEMFC devices. Furthermore, the intricate surface morphology and delicate microstructural architecture of PdRh@PEI remain remarkably intact after prolonged operational exposure, further underscoring the exceptional stability inherent in our engineered catalytic system (Fig. S33).

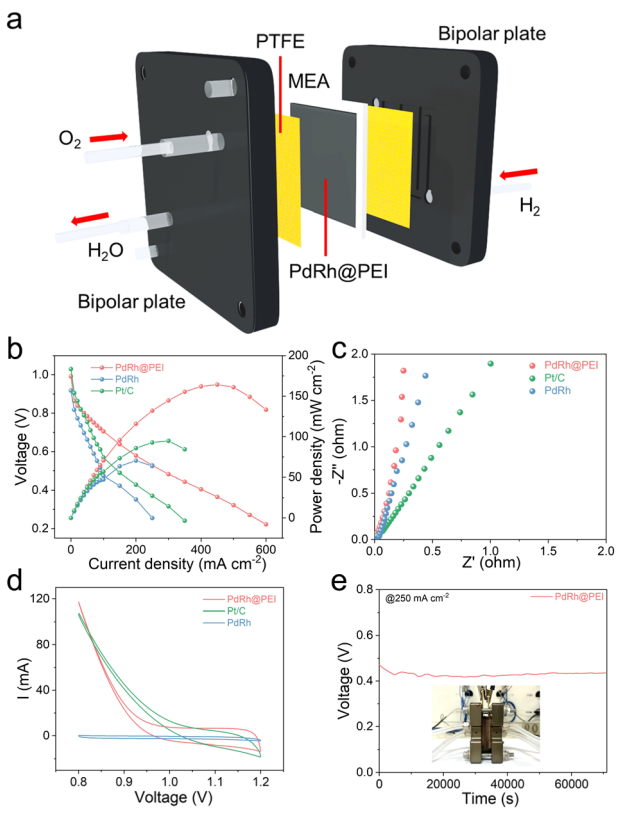

Fig. 5 (a) Schematic illustration of an AEMFC configuration. (b) Polarization curves of MEAs employing the PdRh@PEI metallene, PdRh metallene, and commercial Pt/C as cathode catalysts under H_2–air conditions. (c) EIS spectra, (d) CV curves, and (e) durability performance of the PdRh@PEI metallene cathode at a current density of 250 mA cm^{-2}, and the inset shows the AEMFC photomicrograph.

Conclusions

In summary, the PdRh@PEI metallene has been successfully synthesized through a facile solvothermal reduction approach, exhibiting exceptional ORR activity, remarkable stability, and outstanding resistance to CO and methanol poisoning. Comprehensive electrochemical evaluations reveal that the PdRh@PEI metallene surpasses both the pristine PdRh metallene and commercial Pt/C in alkaline media, demonstrating superior catalytic performance. Specifically, PdRh@PEI demonstrated a $E_{1/2}$ of 0.96 V *vs.* RHE, a mass activity of 1.23 A mg_{Pd}^{-1} at 0.9 V, and negligible variation in $E_{1/2}$ after 10 000 cycles in the ADT test, positioning it among the most advanced ORR catalysts reported under alkaline conditions. Based on the findings of DFT and *in situ* ATR-FTIR analyses, amino-functionalized PEI molecules exert a pronounced electron-donating effect on PdRh atoms, significantly promoting O_2^* dissociation while simultaneously weakening CO* adsorption. This synergistic modulation effectively lowers the energy barrier of the rate-determining step and facilitates the preferential cleavage of *OOH into *O, in contrast to the conventional pathway involving *OOH accumulation, thus breaking the scaling relationship in the conventional oxygen associated mechanism. Importantly, the assembled AEMFC by using the PdRh@PEI metallene as the cathode delivers a higher power density of 164.3 mW cm^{-2} and exhibits continuous and stable performance over 24 h at a current density of 250 mA cm^{-2} under H_2–

air operating conditions. This work would pioneer an effective route for designing molecular interface-mediated metallenes for various catalytic applications.

Author contributions

Shuya Xu: conceptualization, methodology, formal analysis, investigation, and writing – original draft. Yunyi Zhang: formal analysis and validation. Yukun Peng: investigation, data curation. Jiawei Ke: investigation. Xueheng Liu: manuscript modifications, formal validation. Chenglin Yan: writing – review and editing. Lifang Zhang (corresponding author): formal analysis, writing – review and editing. Tongfei Li (corresponding author): validation and writing – review and editing. Tao Qian: supervision, conceptualization.

Conflicts of interest

There are no conflicts to declare.

Data availability

The authors confirm that the data supporting the findings of this study are available within the article or its supplementary information (SI). Supplementary information: details of experimental procedures, additional experimental results, additional theoretical calculation results and Tables S1–S3. See DOI: https://doi.org/10.1039/d5sc07852k.

Acknowledgements

This work was financially supported by the National Natural Science Foundation of China (12204253 and 52502102), the Basic Research Program of Jiangsu (BK20250945), the Natural Science Foundation of the Jiangsu Higher Education Institutions of China (24KJB150026), the Key Research and Development Program of Nantong [No. GZ2024005], the Postgraduate Research & Practice Innovation Program of Jiangsu Province (SJCX25_2024), the Training Programs of Innovation for Undergraduates (202510304023), the Collaborative Innovation Center of Suzhou Nano Science and Technology, the Large Instruments Open Foundation of Nantong University (KFJN2526), and the Nantong University Analysis & Testing Center for their support of the SEM characterization results in this work.

References

1 J. Tian, Y. Song, X. Hao, X. Wang, Y. Shen, P. Liu, Z. Wei, T. Liao, L. Jiang, J. Guo, B. Xu and Z. Sun, *Adv. Mater.*, 2025, **37**, 2412051.
2 Y. Qiu, M. Sun, J. Wu, C. Chai, S. Wang, H. Huang, X. Zhao, D. Jiao, S. Xu, D. Wang, X. Ge, W. Zhang, W. Zheng, B. Huang and Y. Son, *Nat. Commun.*, 2025, **16**, 5262.
3 Z. Cheng, H. Zhang, J. Zhou, X. Chen, L. Yan, R. Zhang and X. Zhou, *Nano Mater. Sci.*, 2025, **5**, 2.
4 X. Yang, Q. Yuan, J. Li, T. Sheng, K. Yao and X. Wang, *Nano Lett.*, 2023, **23**, 3467–3475.
5 P. Han, X. Yang, L. Wu, H. Jia, J. Chen, W. Shi, G. Cheng and W. Luo, *Adv. Mater.*, 2024, **36**, 2304496.
6 J. Wang, B. Zhang, X. Zheng, X. Liu, W. Guo, Z. Luo, Y. Liu, M. Gao, J. Chen, Z. Zhuang, H. Pan and W. Sun, *Nano Res.*, 2024, **17**, 6147–6156.
7 L. Yang, H. Liu, Z. Qiao, P. Sun, D. Li, R. Jiang, S. Liu, Z. Niu, Y. Zhang, T. Lin, Q. Zhang, L. Gu, S. Wang, D. Cao and Z. Chen, *Adv. Energy Mater.*, 2023, **13**, 2204390.
8 Y. Liu, S. Yuan, C. Sun, C. Wang, X. Liu, Z. Lv, R. Liu, Y. Meng, W. Yang, X. Feng and B. Wang, *Adv. Energy Mater.*, 2023, **13**, 2302719.
9 Y. Zhang, Y. Zhao, K. Ye, Y. Zhao, S. Zhou and Y. Yin, *Rare Met.*, 2025, **44**, 1777–1788.
10 X. Hu, Y. Sun, L. Liu, D. Mao and S. Zheng, *Rare Met.*, 2024, **43**, 5835.
11 S. Cai, Q. Wang, N. Zhang, C. Chen, H. Zhang, Y. Feng, L. Duan, Y. Cheng, Z. Meng, H. Li and J. Wu, *Carbon Neutralization*, 2025, **4**, e193.
12 J. Wu, J. Rong, W. Chen, C. Wang, C. Feng, H. Ao, C. Zhu, Y. Zhang and Z. Li, *Rare Met.*, 2025, **44**, 6279–6291.
13 K. Hayashida, J. Nakamura and K. Takeyasu, *Angew. Chem., Int. Ed.*, 2025, **64**, e202502702.
14 C. Jeong, J. Lee, H. Jo, K. Lee, S. Lee, C. Ophus, P. Ercius, E. Cho and Y. Yang, *Nat. Commun.*, 2025, **16**, 8026.
15 Z. Lyu, J. Cai, X. Zhang, H. Li, H. Huang, S. Wang, T. Li, Q. Wang, Z. Xie and S. Xie, *Adv. Mater.*, 2024, **36**, 2314252.
16 Q. Xue, G. Xu, R. Mao, H. Liu, J. Zeng, J. Jiang and Y. Chen, *J. Energy Chem.*, 2017, **26**, 1153–1159.
17 Y. Cao, Y. Liu, X. Zheng, J. Yang, H. Wang, J. Zhang, X. Han, Y. Deng, G. Rupprechter and W. Hu, *Angew. Chem., Int. Ed.*, 2025, **64**, e20242355.
18 H. Nan, B. Chen, L. Mou, Y. Wang and J. Yu, *Coord. Chem. Rev.*, 2025, **542**, 216834.
19 M. Tang, H. Yan, Z. Zheng, H. Zhang, C. Yu, B. Liu and S. Chen, *J. Am. Chem. Soc.*, 2025, **147**, 19931–19940.
20 Y. Chen, Z. Meng, X. Wei, M. Wu, Y. Xiong, H. Tang, R. Wang, T. Tian, D. Wang and H. Tang, *Angew. Chem., Int. Ed.*, 2025, **64**, e202512315.
21 Y. Guo, Q. Wei, F. Wei, H. Liu, H. Zhao, D. Wang and H. Tu, *Rare Met.*, 2024, **43**, 3408–3414.
22 H. Xiong, M. Wiebenga, C. Carrillo, J. Gaudet, H. Pham, D. Kunwar, S. Oh, G. Qi, C. Kim and A. Datyea, *Appl. Catal., B*, 2018, **236**, 436.
23 X. Wang, G. Montaña, M. Spadaro, J. Arbiol, T. Kallio, P. Alanis, Y. Xie and A. Cabot, *ACS Nano*, 2025, **19**, 31384–31394.
24 Y. Zhang, B. Huang, G. Luo, T. Sun, Y. Feng, Y. Wang, Y. Ma, Q. Shao, Y. Li, Z. Zhou and X. Huang, *Sci. Adv.*, 2020, **6**, eaba9731.
25 C. Liang, S. Xing, R. Zhao, X. Hou, T. Chen, Y. Zhao, R. Liu, S. Zhao, X. Wang, X. Guo, N. Xue, L. Peng, X. Zhao, Y. Pei, J. Li and W. Ding, *Chem Catal.*, 2024, **4**, 100849.
26 Y. Peng, X. Zhou, X. Liu, M. Hu, B. Qiu, Y. Jiao, C. D'Agostino, J. Esteban, C. Parlett and X. Fan, *ACS Catal.*, 2025, **15**, 11760–11773.

27 F. Zhou, J. Zhang, Y. Zhang, Y. Wu, Y. Wang and W. Luo, *Coord. Chem. Rev.*, 2024, **509**, 215802.
28 D. Bagchi, M. Riyaz, N. Dutta, G. Chawla, S. Churipard, A. Singh and S. Peter, *Adv. Energy Mater.*, 2024, **14**, 2402237.
29 J. Guo1, Z. Wang, T. Gao and Z. Wang, *Chem. Eng. J.*, 2024, **483**, 149370.
30 Z. Zou, S. Yin, Y. Tang, S. Zhong, L. Wang, S. Xu and H. Liang, *Nano Res.*, 2024, **17**, 8112–8118.
31 X. Lu, J. Wu, X. He, Z. Li, Y. Lu, M. Xu, Y. Qi, Q. Zhang, Y. Liu, M. Du, T. Kamiya, H. Chen and T. Ye, *Nat. Catal.*, 2025, **8**, 536.
32 S. Zhao and Y. Yan, *Rare Met.*, 2025, **44**, 2900–2920.
33 X. Liang, X. Jin, S. Yu, C. Li, C. Song, G. Sheng, X. Ye, R. Gao, L. Lin and D. Ma, *Nat. Commun.*, 2025, **16**, 4159.
34 S. Xie, Y. Lu, K. Ye, W. Tan, S. Cao, C. Wang, D. Kim, X. Zhang, J. Loukusa, Y. Li, Y. Zhang, L. Ma, S. Ehrlich, N. Marinkovic, J. Deng, M. Stephanopoulos and F. Liu, *Environ. Sci. Technol.*, 2024, **58**, 12731–12741.
35 X. Liang, L. Zhang, X. Wang, S. Song and H. Zhang, *Chin. J. Struct. Chem.*, 2023, **42**, 100101.
36 J. Guan, S. Yang, T. Liu, Y. Yu, J. Niu, Z. Zhang and F. Wang, *Angew. Chem., Int. Ed.*, 2021, **133**, 22070–22075.
37 J. Fan, Z. Feng, Y. Mu, X. Ge, D. Wang, L. Zhang, X. Zhao, W. Zhang, D. Singh, J. Ma, L. Zheng, W. Zheng and X. Cui, *J. Am. Chem. Soc.*, 2023, **145**, 5710–5717.
38 T. Chu, P. Tian, G. Wang, Y. Jia, S. Dai, C. Rong, B. Zhang and F. Xuan, *Adv. Mater.*, 2025, **37**, 2504603.
39 Y. Zhou, L. Zhang, M. Wang, X. Shen, Z. Zhu, T. Qian, C. Yan and J. Lu, *Nat. Commun.*, 2025, **16**, 7915.
40 R. Zhang, B. Zhang, J. Lv, Y. Wang, H. Liu, L. Jewell, X. Liu and S. Qiao, *Carbon Neutralization*, 2025, **4**, e70016.
41 S. Jiang, H. Niu, X. An, M. Wang and Y. Cai, *Chem.–Eur. J.*, 2025, e02122.
42 B. Liu, B. Hu, D. Cheng, H. Zang, X. Ge, H. Tan, Y. Wang, X. Duan, Z. Jin, W. Zhang, Y. Li and Z. Su, *Angew. Chem., Int. Ed.*, 2020, **60**, 6076.
43 K. Deng, T. Zhou, Q. Mao, S. Wang, Z. Wang, Y. Xu, X. Li, H. Wang and L. Wang, *Adv. Mater.*, 2022, **34**, 2110680.
44 H. Wang, W. Wang, H. Yu and L. Wang, *Appl. Catal., B*, 2022, **307**, 121172.
45 S. Chang, J. Gao, Y. X uan, D. Li and K. Wang, *Nat. Catal.*, 2025, **5**, 101383.
46 R. Chen, J. Gao, S. Zhao, H. Wang, G. Zhuang, P. Aken, M. Grätzel and J. Luo, *Nat. Catal.*, 2025, **5**, 101389.